EES Batteries

Accepted Manuscript

This article can be cited before page numbers have been issued, to do this please use: E. Sun, G. Zhu, J. Zhao, Z. Ren, B. Wang, Y. Pan, G. Liu and J. Xu, *EES Batteries*, 2026, DOI: 10.1039/D6EB00047A.

View Article Online
DOI: 10.1039/D6EB00047A

Broader context statement

Lithium-ion batteries, owing to their high energy density and fast response, have become a core technology for grid-scale energy storage systems and commercial/industrial energy storage. However, under abuse conditions such as internal short circuits and thermal shocks, thermal runaway may be triggered, leading to rapid heat release and combustible gas emission, thereby posing significant fire and explosion hazards. In this study, we propose the conceptual framework of an active safety protection strategy under a non-flammable refrigerant gas atmosphere and validates its feasibility through experiments, simulations, and thermodynamic analysis. Under near-ambient temperature and atmospheric pressure, the evaporator of a vapor-compression refrigeration cycle is tightly integrated with a sealed battery enclosure. The latent heat of refrigerant phase change is exploited for thermal management, while the in-enclosure nonflammable atmosphere isolates oxygen to suppress secondary combustion of vented gases. In addition, a thermodynamically driven phase-separation mechanism is employed to separate non-refrigerant vent-gas components and enable their controlled discharge. By integrating near-atmospheric phase-change cooling, in-enclosure inerting, and vent-gas separation within a unified concept, this study provides a new perspective for developing active safety protection strategies against lithium-ion battery thermal runaway.

View Article Online
DOI: 10.1039/D6EB00047A

Gas Immersion Enabled Atmospheric-Pressure Near-Ambient Phase-Change Refrigeration Cycle for Active Safety Protection of LFP Battery Thermal Runaway: A Single-Cell Proof of Concept

Enhui Sun[a,b,*], Guangwei Zhu[a,b], Jinyang Zhao[a,b], Zixin Ren[a,b], Bowen Wang[a,b], Yuning Pan[a,b], Guohua Liu[b], Jinliang Xu[b]

a) Yanzhao Electric Power Laboratory of North China Electric Power University, North China Electric Power University, Baoding 071003, Hebei, China

b) Key Laboratory of Power Station Energy Transfer Conversion and System, North China Electric Power University, Ministry of Education, Beijing, 102206, China

* Corresponding Author: Enhui Sun (ehsun@ncepu.edu.cn).

Abstract

Gas venting during thermal runaway of lithium iron phosphate cells can lead to flaming combustion of combustible vent gases, creating severe fire hazards. This study originally proposes the conceptual framework of an active safety protection strategy under a non-flammable refrigerant gas atmosphere, and validates its feasibility through a combination of experiments, simulations, and thermodynamic analysis. The evaporator of a vapor-compression refrigeration cycle is conceptually integrated with a sealed battery enclosure. By screening working fluids, determines a non-flammable refrigerant with a saturation temperature slightly below ambient temperature at atmospheric pressure, achieving a coupled function of active cooling, atmospheric inerting, and safe gas discharge. Under normal operation, the refrigerant evaporates in a cold plate to absorb heat for thermal management, while maintaining a non-flammable atmosphere in the enclosure. During thermal runaway, the refrigerant gas suppresses combustion reactions and entrains the vent gas into a gas-liquid separator, where flammable components are separated and discharged safely. Explosion-limit tests show that increasing the volumetric fraction of trans-1-Chloro-3,3,3-trifluoropropene(R1233zd(E)) in hydrogen mixtures markedly narrows the flammability range, with no combustion observed when the fraction exceeds 95%. Single-cell thermal runaway experiments on a 28 Ah lithium iron phosphate cell show that no visible flaming combustion of the vented gases was observed under the tested refrigerant atmosphere. Numerical simulations of gas-liquid separation indicate that the two-phase flow field inside the separator is uniformly distributed, enabling continuous and efficient separation of the

gases generated during thermal runaway. Thermodynamic calculations show that, at an evaporation temperature of 20 °C and a condensation temperature of 60 °C, this refrigerant exhibits the best cycle performance among all candidate working fluids, achieving a coefficient of performance of 4.85. Overall, the results demonstrate the feasibility of suppressing secondary vent-gas combustion in a single-cell lithium iron phosphate configuration.

Keywords: Battery thermal runaway; Active safety; Vapor-compression refrigeration; Non-flammable gas atmosphere; Gas-liquid separation

1. Introduction

Driven by the rapid penetration of renewable energy and the growth of high-power loads, electrochemical energy storage has become a key enabling technology for the energy transition.[1] Among available options, lithium-ion batteries are widely deployed in grid scale storage and transportation electrification due to their high energy density and long cycle life.[2] However, under abusive conditions (e.g., internal short circuits and thermal shocks), high energy density cells are prone to thermal runaway (TR).[3] The intense heat release and jetting of flammable gases during thermal runaway can readily initiate module-level and even system-level propagation, posing a critical safety challenge for energy storage facilities.

Thermal runaway vent gas mainly consists of hydrogen, carbon monoxide, and light hydrocarbons.[4,5] Hydrogen, in particular, has an extremely low lower flammability limit and a high flame-propagation speed,[6,7] making it a key contributor to deflagration and explosion incidents in battery energy storage stations. Accident investigations have shown that gas accumulation and instantaneous ignition often occur at an early stage, before fire-suppression systems are activated. Conventional strategies that trigger extinguishing or venting based on smoke, temperature, or pressure thresholds therefore struggle to interrupt accident escalation in time.[8,9] Accordingly, actively preventing gas accumulation and flame propagation during thermal runaway—by controlling the enclosure atmosphere—is a central challenge in safety-oriented energy storage design.

Current academic efforts on preventing and controlling lithium-ion battery thermal runaway largely aim to establish full-life-cycle safety barriers[10] and can be broadly grouped into three core directions: (i) suppressing TR initiation, (ii) suppressing TR propagation, and (iii) fire extinguishing and explosion mitigation technologies

The first direction focuses on preventing TR initiation, primarily by enhancing thermal management capability to avoid heat accumulation that drives cells into an unstable state. Toward this end, Hwang et al.[11] systematically reviewed and compared mainstream thermal management approaches—such as air cooling, liquid cooling, and phase-change cooling—and concluded that liquid cooling offers advantages in both cooling effectiveness and

temperature uniformity. Building on this foundation, Zhou et al.[12] optimized the structural design of liquid-cooling systems from an engineering implementation perspective. For large-capacity maritime applications, Tian et al.[13] demonstrated that a wavy microchannel configuration can markedly mitigate localized hot spots. To overcome the limitations of conventional cooling under high-rate fast charging, Wahab et al.[14] noted that, compared with indirect liquid cooling, immersion cooling enables direct contact between the coolant and cell surface, thereby substantially reducing interfacial thermal resistance and improving temperature uniformity, representing a promising evolutionary pathway for suppressing TR initiation. However, although high-efficiency thermal management can effectively limit temperature rise under normal operating conditions, external cooling is often unable to arrest the internal chain reactions once mechanical abuse or a severe internal short circuit triggers an abrupt and intense heat release. As a result, single-cell thermal runaway remains difficult to fully prevent under extreme conditions.

Given the practical inevitability of single-cell failure, the second research stream has shifted toward suppressing thermal runaway propagation, aiming to interrupt heat-transfer pathways through module-level structural design and/or thermal barriers. Feng[10] reported that, at the system level, effective strategies include thermal insulation, enhanced heat dissipation, and rapid discharge of adjacent cells. From a materials perspective, Wong and Sun et al.[15,16] respectively demonstrated the insulating performance of nanofiber aerogel composites and ceramic fiber felts. Chen et al.[17] further proposed a “sandwich” architecture that couples a flame-retardant phase-change material with aerogel felt. Experiments showed that this design mitigates thermal shock by absorbing heat via phase change while the aerogel layer provides thermal insulation, thereby completely blocking propagation even at reduced module spacing. This offers a promising route to reconcile the trade-off between lightweight design and safety. Nevertheless, passive thermal barriers inevitably face limits in heat resistance and impact tolerance. Studies indicate that their primary benefit is to delay propagation on the order of tens of seconds to several minutes.[18,19] The effective protection time is constrained by material thickness and heat capacity. When the energy release during thermal runaway is sufficiently intense—exceeding the barrier’s protection threshold—or when high-pressure gas jets induce open flames, passive isolation can fail. In such cases, active mitigation measures must be introduced.

Therefore, the third research stream emphasizes fire suppression and explosion mitigation as the final line of defense when heat-propagation control fails. To address existing fire and explosion hazards, Hu[20] showed that fine water mist can delay thermal runaway evolution through the combined mechanisms of rapid cooling and oxygen isolation. Numerical simulations by Dhuchakallaya et al.[21] further suggest that using inert gases (e.g., nitrogen) as cooling media can enhance heat removal while reducing oxygen participation, thereby lowering the likelihood of

View Article Online
DOI: 10.1039/D5EE03047A

combustion during thermal runaway. Deng et al.[22] subsequently verified the high efficiency of composite extinguishing agents. To cope with extreme scenarios involving explosions and jet fires, recent studies have begun exploring smart materials that provide both ablation resistance and active cooling. For example, Wang et al.[23] developed a composite hydrogel with an ultrahigh silica loading. When exposed to high temperatures, it can in situ form a rigid ceramic-like protective layer while continuously absorbing heat through evaporation, effectively resisting erosion by high-pressure jet flames. These advances indicate that multi-mechanism, synergistic fire extinguishing and explosion mitigation approaches can substantially reduce the consequences of post-runaway accidents.

Experimental and field measurements show that the high temperature and flammable gases produced during thermal runaway can accumulate within seconds.[24,25] Under extreme conditions, existing thermal management and fire-suppression technologies often respond too slowly to effectively curb rapid gas buildup and flame spread during thermal runaway. Consequently, for high-power, large-capacity applications, safety remains a key bottleneck limiting large-scale deployment.

To suppress thermal runaway initiation and inhibit gas combustion as well as flammable gas accumulation during thermal runaway, this paper puts forward an active safety protection strategy. The strategy combines atmospheric-pressure near-ambient vapor-compression refrigeration cycle with sealed battery enclosure, achieving coordinated active cooling, atmospheric inerting and safe venting functions. A single lithium iron phosphate cell test is conducted to verify the proposed concept. First, a non-flammable refrigerant is selected whose saturation temperature at 1 atm is slightly below ambient. A vapor-compression cycle is then established: phase-change heat absorption in a liquid cold plate provides high-efficiency thermal management, while the gaseous refrigerant continuously maintains a non-flammable atmosphere inside the atmospheric-pressure enclosure. Once thermal runaway is triggered, the refrigerant gas suppresses combustion reactions and entrains the vented products into the refrigeration loop. A gas-liquid separator subsequently removes flammable constituents, enabling controlled and safe discharge. Explosion-limit tests, thermodynamic calculations, gas-liquid separation simulations, and single-cell thermal runaway experiments are used to evaluate the feasibility of this concept.

2. Methodology and Working-Fluid Screening

2.1 Active protection method for battery thermal runaway based on a non-flammable refrigerant atmosphere

This study proposes an active safety protection method for lithium-ion batteries by deeply coupling a vapor-

compression refrigeration cycle with atmosphere control in a sealed battery enclosure. As shown in Fig. 1, the system consists of a sealed battery enclosure, compressor, condenser, expansion valve, liquid cold plate, and a gas-liquid separator. During operation, low-pressure refrigerant vapor in the enclosure enters the compressor and is compressed to a higher pressure. The compressed refrigerant then flows into the condenser, where it condenses into a high-pressure liquid. The liquid subsequently enters the gas-liquid separator, which enables phase separation and the discharge of non-refrigerant gases. After throttling through the expansion valve, the liquid refrigerant expands to a low pressure and enters the liquid cold plate. Inside the cold plate, the refrigerant undergoes liquid-vapor phase change to absorb heat efficiently. Any refrigerant that is not fully vaporized is recovered via a receiver for reuse, while the gaseous refrigerant establishes a stable non-flammable atmosphere within the enclosure. Overall, the system integrates high-efficiency phase-change cooling, atmospheric inerting, and flammable-gas separation.

(1) High-efficiency phase change cooling: After expansion, the liquid refrigerant enters the cold plate. Refrigerant that remains partially liquid at the cold-plate outlet is collected in the receiver and recycled. Meanwhile, the refrigerant boils in the flow channels under near-atmospheric conditions, absorbing a large amount of latent heat of vaporization. This in-plate phase-change heat absorption effectively reduces the battery temperature rise and local hot spots, improves temperature uniformity, and delays the onset of thermal runaway.

(2) Atmospheric inerting and flame retardancy: The refrigerant absorbs heat in the liquid cold plate, evaporates, and then diffuses into the sealed battery enclosure to establish a non-flammable refrigerant-vapor atmosphere. The vapor-compression loop continuously recirculates and reuses the refrigerant, while the gas-liquid separator removes non-refrigerant gases, thereby persistently diluting the oxygen concentration and stabilizing the refrigerant-gas fraction within the enclosure. Consequently, when thermal runaway occurs, the enclosure atmosphere can effectively suppress combustion reactions and reduce the risk of fire.

(3) Flammable-gas separation: During thermal runaway, the refrigerant entrains the vented products into the refrigeration loop and delivers them—after compression—to the condenser. At a prescribed condenser outlet temperature and pressure, the refrigerant, with a relatively high saturation temperature, preferentially condenses and exits as a liquid. In contrast, key vent-gas components such as H_2, CO, and light hydrocarbons have critical temperatures far below the condenser outlet temperature and therefore remain in the gas phase. This difference enables efficient separation of liquid refrigerant from flammable gases. The condensed refrigerant collects at the separator bottom and returns to the cold plate through the expansion valve, forming a closed-loop working-fluid circuit, whereas the gaseous flammable components are routed from the separator gas outlet for safe discharge.

View Article Online
DOI: 10.1039/D6EB00047A

2.2 Refrigerant screening

To enable coupled operation of the refrigeration loop and enclosure atmosphere control, the refrigerant must satisfy both cooling-performance and safety-protection constraints. Priority is given to non-flammability and low toxicity. In addition, the saturation temperature at atmospheric pressure should be slightly below the typical ambient temperature of the battery enclosure and ideally fall within 0-20 °C, so that efficient evaporative heat absorption can be achieved via phase change under near-1 atm conditions. Based on these criteria, Fig. 2(a) presents the preliminary screening results for several non-flammable refrigerants.

A temperature-matching screening was first performed using an atmospheric-pressure saturation-temperature window of 20 °C, which identified three candidate working fluids: trans-1-chloro-3,3,3-trifluoropropene (R1233zd(E)), cis-1-chloro-2,3,3,3-tetrafluoropropene (R1224yd(Z)), and 1,1,1,3,3-pentafluoropropane (R245fa). Their key thermophysical properties are summarized in Table 1. The saturation temperatures at 1 atm are 18.263 °C, 14.617 °C, and 15.048 °C for R1233zd(E), R1224yd(Z), and R245fa, respectively. Notably, these candidates differ in safety classification and environmental impact: R1233zd(E) and R1224yd(Z) are A1-class refrigerants with low global warming potential (GWP), whereas R245fa exhibits a substantially higher GWP.

To illustrate the cycle process of the candidate working fluids in the proposed system, R1233zd(E) is taken as an example. Its phase diagram and the corresponding P–h diagram of the vapor-compression cycle are shown in Fig. 2(b). For the representative operating condition considered in this study, the evaporation temperature and condensation temperature are specified to 20 °C and 60 °C, respectively. The corresponding evaporating and condensing pressures are then determined from the saturation properties of each working fluid. For R1233zd(E), these pressures are approximately 0.1 MPa and 0.4 MPa, respectively. Under these conditions, the refrigerant in the sealed enclosure is predominantly low-pressure saturated vapor. It is compressed by the compressor into high-pressure superheated vapor, with both pressure and temperature increasing. The refrigerant then rejects heat to the external cooling medium in the condenser and condenses into a high-pressure liquid. The condensed working fluid subsequently enters the gas-liquid separator, where the liquid refrigerant is recovered for reuse and non-refrigerant gases are separated. The liquid refrigerant then undergoes isenthalpic expansion through the expansion valve, resulting in a reduction in pressure and temperature, before entering the liquid cold plate. There, it boils and vaporizes within the flow channels, absorbing heat from the battery. The resulting vapor returns to the sealed enclosure to re-establish the non-flammable atmosphere, thereby completing the closed-loop cycle.

2.3 Comparative analysis of vapor-compression cycle characteristics for different working fluids

To highlight the cycle-level differences between novel non-flammable refrigerants and conventional refrigerants within the temperature window relevant to battery thermal management, a thermodynamic model of a vapor-compression refrigeration cycle was established under identical boundary conditions. The cycle characteristics of different working fluids were then compared based on their P-h diagrams. As shown in Fig. 3, P_e denotes environmental pressure, the four principal thermodynamic state points of the cycle are defined as follows: state 1 is the compressor inlet, where the refrigerant is low-pressure saturated vapor; state 2 is the compressor outlet, where the refrigerant is high-pressure superheated vapor; state 3 is the condenser outlet, where the refrigerant is high-pressure liquid; and state 4 is the liquid-cold-plate inlet, where the refrigerant is a low-pressure two-phase mixture. Figure 3(a) shows a conventional closed vapor-compression refrigeration cycle, in which the refrigerant circulates only within the refrigeration loop and the low-pressure evaporator is isolated from the battery enclosure. In this configuration, the refrigerant mainly serves as a heat-transfer working fluid and does not participate in enclosure atmosphere control. Figure 3(b) is termed a near-atmospheric-pressure coupled cycle because the low-pressure side of the refrigeration loop is directly coupled with the sealed battery enclosure, while the refrigerant still circulates in a closed loop rather than being discharged to the ambient environment. At an evaporation temperature of 20 °C and a condensation temperature of 60 °C, the conventional refrigerant R134a operates overall in a relatively high-pressure range. In contrast, the pressure level of the R1233zd(E) cycle shifts downward, with an evaporation pressure close to 1 atm, enabling liquid–vapor phase change under near-atmospheric conditions and thus facilitating direct coupling with the sealed battery enclosure. Therefore, compared with traditional refrigerants, the operating temperature range of battery energy-storage systems is better matched to R1233zd(E). This refrigerant can maintain efficient cooling while reducing compressor power consumption due to its near-atmospheric evaporation and lower pressure ratio. These cycle characteristics align well with the coupled-operation objectives of the proposed system and provide a thermodynamic basis for subsequent energy-efficiency evaluation and safety analysis under thermal runaway conditions.

3. Experimental and numerical methods

This section describes the experimental and computational methods used in this study. The overall workflow comprises four parts. First, explosion-limit tests were conducted according to EN 1839, Method B[26] to quantitatively evaluate the inerting capability of R1233zd(E) in H_2/air mixtures. Second, overcharge-triggered thermal runaway tests were performed under air and R1233zd(E) atmospheres; the flame-suppression performance was assessed based

on temperature, expansion force, and ignition response. Third, numerical simulations were carried out to investigate the two-phase separation of liquid R1233zd(E) and flammable vent gases within the gas–liquid separator. Finally, a thermodynamic and exergy analysis model of the vapor-compression refrigeration cycle was developed to calculate the cooling capacity, COP, and component-wise exergy destruction, providing a basis for working-fluid selection and system design.

3.1 Explosion-limit experimental setup and procedure

The explosion-limit test apparatus is presented in Fig. 4. The experimental system consists of a gas metering and distribution unit, a reaction vessel, an ignition system, a temperature-control unit, and a pressure acquisition system. The reaction vessel is a 6 L cylindrical tube-type chamber.

To ensure homogeneous mixing, a magnetic stirrer was placed at the bottom of the vessel. The spark-ignition system operated at a discharge voltage of 15 kV with a spark duration of 0.4 s. The vessel pressure was measured using a pressure transducer with an accuracy of 0.1% full scale (FS). The temperature was controlled to within ±0.2 ^{o}C, and the gas-mixing accuracy was 0.1%. The inlet air was dried by passing it through a glass drying tube packed with indicating silica gel and molecular sieves. The hydrogen purity was ≥ 99.999%, and the R1233zd(E) purity was ≥ 99.8%.

All tests were conducted at an ambient pressure of 1 atm, with the initial gas temperature in the vessel set to 30 ^{o}C. Before each run, the vessel was evacuated to below 3 kPa. The test mixture was then prepared according to Dalton's law of partial pressures, sequentially charging H_2, R1233zd(E), and air to their prescribed partial pressures. After filling, the magnetic stirrer was activated to homogenize the mixture, followed by a 5 min settling period. Spark ignition was then triggered while the vessel pressure history was recorded. An explosion was deemed to occur at a given composition when the post-ignition pressure rise satisfied $\Delta P/P_0 \geq 5\%$, where P_0 is the absolute pressure at the instant of ignition. Each condition was repeated more than three times to ensure accuracy and reproducibility.

To validate the test apparatus and the adopted criterion, the explosion limits of H_2 in dry air were measured at 30 ^{o}C and compared with literature values[27]. The lower explosion limit (LEL) and the upper explosion limit (UEL) represent the lowest and highest concentrations, respectively, at which a mixture of combustible gas or vapor and air can explode. The results show relative deviations of 0.22% for the LEL and 2.51% for the UEL, confirming the reliability of the experimental platform.

3.2 Thermal runaway experimental setup and procedure

A 28 Ah $LiFePO_4$ cell was used in this study. The charge and discharge cutoff voltages were 3.65 V and 2.5 V,

respectively. Prior to testing, the cell underwent two formation cycles at a 0.5 C charge rate for activation, and was then charged to 100% SOC. The thermal runaway experimental setup is shown in Fig. 5. During the test, the cell was mounted vertically on a lift platform and secured with clamps. A spoke-type load/force sensor was installed between the two clamps to monitor the variation in cell expansion force during thermal runaway. Thermal runaway was triggered by overcharge. Temperatures were measured using K-type thermocouples: T_1 and T_2 were positioned 10 cm and 20 cm above the cell's safety valve, respectively, while T_3–T_5 were attached to the cell surface. To evaluate the flammability of the vented gases under different atmospheres, an electric igniter was placed directly above the safety valve and activated during the vigorous venting stage to observe the ignition and combustion response.

Thermal runaway tests were conducted under two different atmospheric configurations: an outdoor open-air condition and a sealed chamber filled with high-concentration R1233zd(E), in which the oxygen concentration was below 1%. This arrangement was mainly adopted for safety considerations. During thermal runaway in a confined and sealed battery compartment, a large amount of flammable vent gas may be released and accumulated. When these gases mix with air and come into contact with an ignition source, a significant deflagration risk may be introduced. Therefore, the air-atmosphere test was conducted in an outdoor open configuration to reduce the accumulation of flammable gases and mitigate the risks to test personnel and experimental facilities. Because the two experiments differed simultaneously in chamber geometry, convective heat dissipation, ignition environment, and other boundary conditions, this comparison is intended as a proof-of-concept evaluation of flame suppression under a high-concentration R1233zd(E), oxygen-deficient environment.

For both conditions, a preload of 2000 N was applied prior to testing. Because the normal boiling point of R1233zd(E) at 1 atm is approximately 18.3 °C, the chamber was equipped with an air-conditioning to prevent refrigerant condensation. Before each test, the chamber temperature was maintained at approximately 25 °C to ensure that the refrigerant remained in the gaseous phase. An oxygen concentration monitor was used to continuously monitor the oxygen concentration. Once the oxygen level decreased to below 1% and stabilized, the cell was overcharged to trigger thermal runaway. When vigorous venting occurred, an electric igniter was activated to document the ignition or suppression behavior under the two atmospheres.

3.3 Numerical method for gas-liquid separation

In this study, ANSYS Fluent was used to numerically simulate the separation process of liquid R1233zd(E) from flammable gases (H_2, CH_4, C_2H_4, and CO) in the gas-liquid separator, with the aim of evaluating the separator's adaptability to the operating conditions required for refrigerant recovery and safe discharge of flammable components.

Because the liquid level and its transient fluctuations are key indicators of separator performance, it is necessary to resolve the location and evolution of the gas-liquid interface. The Volume of Fluid (VOF) method can accurately capture interfacial morphology and its time-dependent evolution and has been widely applied in multiphase-flow simulations.[28] Therefore, the VOF model was adopted here to track and compute the evolution of the gas-liquid interface.

Continuity equation:

$$\frac{\partial \rho}{\partial t} + \nabla(\rho u) = 0 \tag{1}$$

where u is the mixture velocity vector.

The mixture density ρ is calculated as:

$$\rho = \alpha_g \rho_g + (1 - \alpha_g)\rho_l = 0 \tag{2}$$

where α_g, ρ_g, and ρ_l denote the gas volume fraction, gas-phase density, and liquid-phase density, respectively.

The volume fraction constraint for the two-phase system is:

$$\alpha_g + \alpha_l = 1 \tag{3}$$

where α_l is the liquid volume fraction

The momentum conservation equation is written as:

$$\frac{\partial \rho u}{\partial t} + \nabla(\rho u u) = -\nabla \rho + \nabla\left[\mu\left(\nabla u + \nabla u^{\mathrm{T}}\right)\right] + \rho g + F \tag{4}$$

where μ is the dynamic viscosity, and F represents the source term in the momentum equation arising from surface tension and wall adhesion effects.

The standard k-ε turbulence model, known for its numerical robustness and reliable accuracy, was employed to capture the main characteristics of turbulence.

3.4 Thermodynamic calculation method

3.4.1 Energy balance model

To facilitate a comparative evaluation of cycle performance for different working fluids, a thermodynamic model of the vapor-compression refrigeration cycle was developed. For simplicity, the theoretical-cycle calculations were performed under the following assumptions[29]: (1) The refrigerant at the evaporator outlet is saturated vapor; (2) Pressure losses due to fluid flow are neglected throughout the cycle; (3) Except in the two heat exchangers, the

View Article Online
DOI: 10.1039/D6EB00047A

refrigerant is assumed to have no heat exchange with the surroundings along the cycle.

Here, $q_{m,1}$, $q_{m,2}$, and $q_{m,4}$ represent the refrigerant mass flow rates at states 1, 3, and 4, respectively. Under the ideal steady-state cycle assumptions adopted in this work, the refrigerant mass flow rate is identical at all state points, i.e., $q_{m,1}= q_{m,2}= q_{m,3}= q_{m,4}$.

The system cooling capacity is given by:

$$Q_e = q_{m,4}(h_1 - h_4) \tag{5}$$

The compressor input power is calculated as:

$$W_c = q_{m,1}(h_2 - h_1) \tag{6}$$

The coefficient of performance (COP) of the cycle is defined as:

$$\mathrm{COP} = \frac{Q_e}{W_c} \tag{7}$$

3.4.2 Exergy balance model

Exergy analysis based on the second law of thermodynamics, enables a quantitative evaluation of the irreversibilities in each system component and their relative contributions, thereby identifying the key links for improving energy efficiency.

For a typical vapor-compression refrigeration system, changes in kinetic and potential energies can be neglected. The specific physical exergy at each state point can be expressed as:

$$e_x = [(h_x - h_0) - T_0(s_x - s_0)] \tag{8}$$

where h_0 and s_0 are the refrigerant enthalpy and entropy at the reference state, defined as T_0=298.15 K and P_0=101.325 kPa.

The exergy destruction in the compressor is:

$$E_{D,COM} = W_c - q_{m,1}(e_2 - e_1) \tag{9}$$

where W_c is the compressor power consumption.

The exergy destruction in the condenser is:

$$E_{D,CON} = q_{m,3}(e_2 - e_3) \tag{10}$$

The exergy destruction in the expansion valve is:

$$E_{D,T} = q_{m,4}(e_3 - e_4) \tag{11}$$

View Article Online
DOI: 10.1039/D6EB00047A

The exergy destruction in the liquid cold plate (evaporator) is:

$$E_{\mathrm{D,L}} = q_{m,1}(e_4 - e_1) - Q_{\mathrm{e}}\left(\frac{T_0}{T_{\mathrm{e}} + \Delta T} - 1\right) \tag{12}$$

Where ΔT denotes the temperature difference between the cooled object and the refrigerant and is fixed at 5 °C.

The total exergy destruction of the system is:

$$E_{\mathrm{D,tot}} = \sum_{i=1}^{k} E_{\mathrm{D,i}} \tag{13}$$

The exergy efficiency of the system is defined as:

$$\eta_{\mathrm{ex}} = 1 - \frac{E_{\mathrm{D,tot}}}{W_{\mathrm{c}}} \tag{14}$$

4. Results analysis

4.1 Analysis of explosion limit experimental results

Given the complex composition of gases released during lithium-ion battery thermal runaway and the pronounced variability in their flammability, hydrogen was selected as a representative component to validate the inerting performance. Hydrogen typically accounts for a relatively high proportion of thermal runaway vent gases[30,31] and is characterized by a low lower explosion limit and a high flame propagation velocity, making it the most readily ignitable and thus a critical combustible species. Therefore, if an H_2/air mixture can be suppressed to a nonflammable state under a high volumetric fraction of R1233zd(E), a conservative basis can be established to argue that the mixed gases generated during thermal runaway will also remain nonflammable under the same inerting conditions.

As shown in Fig. 6, at 30 °C and 1 atm, the LEL and UEL of the mixture were determined by varying the volumetric fraction of R1233zd(E) in the binary R1233zd(E)-H_2 system. With increasing R1233zd(E) volume fraction, the UEL decreased markedly, whereas the LEL increased only gradually. Consequently, the explosion limit range of the mixture progressively narrowed, indicating that the addition of R1233zd(E) can effectively inhibit hydrogen combustion. It should be noted that occasional explosions were still observed outside the nominal flammability range. This behavior is mainly attributed to the fact that, near the upper limit, the combustion of the fuel-air mixture is in a critical and unstable regime and is highly sensitive to local fluctuations in composition, thereby leading to sporadic explosive events.

When the volumetric fraction of R1233zd(E) in the R1233zd(E)/H_2 mixture reached 95%, the UEL and LEL curves intersected, suggesting that the system could no longer sustain combustion. Upon further increasing the

View Article Online
DOI: 10.1039/D5EE00647A

R1233zd(E) fraction, no stable explosive response was observed; the mixture can therefore be regarded as nonflammable in air over the entire composition range. These results demonstrate that a high-concentration R1233zd(E) atmosphere can effectively suppress the combustion of gases generated during thermal runaway. Moreover, effective inhibition was achieved even for hydrogen, the most readily ignitable component, providing experimental evidence to support the nonflammability of thermal runaway vent gases under high R1233zd(E) concentrations.

4.2 Analysis of experimental results on battery thermal runaway

Figures 7 and 8 present the overcharge-triggered thermal runaway responses of a 28 Ah $LiFePO_4$ cell under two different test configurations: an outdoor open-air condition and a sealed chamber filled with high-concentration R1233zd(E), in which the oxygen concentration was below 1%. *F* denotes the cell expansion force measured by the force sensor. Its initial value corresponds to the applied preload of 2000 N, and its subsequent variation reflects the evolution of the cell expansion force during thermal runaway. *U* denotes the cell voltage. *T* refers to the temperature of the battery surface and the area above the safety valve. In the following, the key characteristic parameters and phenomena during thermal runaway are analyzed based on the evolutions of temperature, expansion force, and voltage. It should be noted that, because the two tests differed simultaneously in chamber geometry, convective heat dissipation, gas confinement, and ignition environment, the comparison between Figs. 7 and 8 is intended to provide a proof-of-concept evaluation of flame suppression under a high-concentration R1233zd(E), oxygen-deficient environment, rather than to independently quantify the specific contribution of R1233zd(E) relative to generic oxygen-displacement effects.

As shown in Fig. 7, under an air atmosphere, continuous overcharge intensified internal side reactions accompanied by gas generation, leading to a sustained rise in internal expansion force. At 1280 s, the expansion force reached the safety threshold, and the safety valve opened, instantaneously releasing a large amount of white smoke, which mainly consisted of organic solvents evaporated from the electrolyte. After vent opening, the overcharge continued and both the cell temperature and voltage gradually increased. Starting at 9210 s, the cell voltage dropped sharply, indicating that violent internal reactions caused an internal short circuit, marking the onset of thermal runaway. At 9458 s, a large amount of gas was released; the vented combustible components were rapidly ignited and continued to burn for approximately 302 s. During thermal runaway, the maximum cell surface temperature reached 144 °C, while the peak temperature above the safety valve reached 781.2 °C. This pronounced temperature

View Article Online
DOI: 10.1039/D6EE00047A

difference indicates that, in air, vigorous combustion of thermal runaway vent gases substantially increases the heat release, thereby amplifying the thermal hazard of the battery system.

As shown in Fig. 8, under an R1233zd(E) atmosphere, although overcharge could still trigger internal reactions and induce thermal runaway, the smoke released from the safety valve was not ignited under repeated ignition attempts. Under this condition, the maximum cell surface temperature was 183.2 °C, whereas the maximum temperature above the safety valve was only 88.8 °C. In comparison, under the outdoor open-air condition, the maximum cell surface temperature was 144 °C, while the peak temperature above the safety valve reached 781.2 °C. These results indicate that, in a high-concentration R1233zd(E) environment, the combustion of thermal runaway vent gases can be effectively suppressed by isolating oxygen.

Under the tested high-concentration R1233zd(E) environment, the temperature above the safety valve was significantly reduced, mainly because secondary flaming combustion of the vented gases did not occur. The relatively higher cell surface temperature under the high-concentration R1233zd(E) condition may be attributed to the different boundary conditions between the two tests. The air test was conducted in an outdoor open environment, which allowed stronger convective heat dissipation and dilution of hot gases. In contrast, the R1233zd(E) test was performed in a sealed chamber, where heat dissipation was more limited and hot vent gases could remain near the cell.

The gas composition measured by gas chromatography (GC), with N_2 excluded, is shown in Fig. 9. The gases released after thermal runaway of the lithium-ion cell mainly consisted of nonflammable CO_2 and combustible species such as H_2, CO, C_2H_4, CH_4, and C_2H_6, along with a small amount of other hydrocarbons (C_xH_y). Among them, CO_2 accounted for 29.8 vol%. The formation of CO_2 is primarily associated with the decomposition of the solid electrolyte interphase (SEI) and the thermal decomposition of carbonate solvents in the electrolyte, including DMC, DEC, and EMC.[32] Hydrogen was the most abundant component (47.86 vol%) and mainly originated from reactions between lithium and the binder in the electrolyte; the corresponding reaction equation is as follows:[33]

$$2Li + H_2O \rightarrow Li_2O + H_2 \tag{15}$$

$$-CH_2 - CF_2 - + Li \rightarrow LiF + -CH = CF + 0.5H_2 \tag{16}$$

The volumetric fraction of CO was 7.4%. In $LiFePO_4$ (LFP) cells, CO is mainly produced via two pathways: (i) reduction of CO_2 to CO on the anode surface (Eq. 17); and (ii) reaction between the electrolyte and O_2 released from the thermal decomposition of the cathode active material at elevated temperatures (Eqs. 18–20)[34,35]. In addition, other hydrocarbons (C_xH_y) are primarily generated from the reductive decomposition of the SEI film and reactions between the anode and the electrolyte under high-temperature conditions[36].

View Article Online
DOI: 10.1039/D6EB00047A

$$C_2H_5OCOOCPF_4 \rightarrow PF_3O + CO_2 + C_2H_5F \quad (17)$$

$$2.5O_2 + C_3H_4O_3(\text{EC}) \rightarrow 3CO_2 + 2H_2O \quad (18)$$

$$6O_2 + C_5H_{10}O_3(\text{DEC}) \rightarrow 5CO_2 + 5H_2O \quad (19)$$

$$3O_2 + C_3H_6O_3(\text{DMC}) \rightarrow 3CO_2 + 3H_2O \quad (20)$$

4.3 Analysis of gas-liquid separation simulation results

The phase-separation process between R1233zd(E) and representative thermal runaway vent gases inside the gas-liquid separator is illustrated in Fig. 10. Figure 10(a) shows the contour map of the volumetric fraction of R1233zd(E) within the separator. Under 60 °C and 0.4 MPa, R1233zd(E) in the mixed working fluid remains in the liquid phase. After the mixture enters the separator, a pronounced non-uniform region forms near the inlet. As the inflow continues and the flow decelerates inside the separator, a stable stratified structure gradually develops in the main region under gravity. The lower part of the separator is dominated by a high-volume-fraction liquid phase, whereas the upper part is dominated by the gas phase. The gas-liquid interface is clear and continuous, indicating good gravitational separation performance.

To further characterize the time scale and stability of the separation process, Fig. 10(b) presents the axial profiles of the R1233zd(E) volumetric fraction along the separator centerline at different times. In the initial stage, inlet jet impingement and recirculation lead to pronounced axial fluctuations in the centerline volume fraction. With increasing time, the overall fluctuation amplitude decreases, and the phase interface becomes progressively sharper. This indicates that the separator can maintain a stable gravity-driven separation process under continuous feeding, thereby enabling liquid refrigerant recovery while continuously discharging the gaseous vent products. Overall, the numerical simulations confirm that the proposed gas-liquid separator can continuously separate liquid R1233zd(E) from thermal runaway vent gases, meeting the requirement for continuous extraction and controlled release of combustible components during the thermal runaway event.

4.4 Analysis of thermodynamic calculation results

The thermophysical properties of the refrigerants were obtained from REFPROP 10.0. Based on the energy and exergy analysis models of the vapor-compression refrigeration cycle described above, the performance metrics of the candidate working fluids under typical battery thermal management conditions were calculated and compared, including COP, W_c, total system exergy destruction, and exergy efficiency, to evaluate their overall thermodynamic

View Article Online
DOI: 10.1039/D6EB00047A

performance.

4.4.1 Performance analysis of candidate working fluids

Figure 11 illustrates the variations in COP, W_c, total exergy destruction, and exergy efficiency of R1233zd(E), R1224yd(Z), and R245fa with condensation temperature. In general, as the condensation temperature increases, both COP and exergy efficiency decrease for all three refrigerants, whereas W_c and the total exergy destruction increase. This trend mainly arises because a higher condensation temperature leads to an elevated condensing pressure and a larger cycle pressure ratio, thereby intensifying compressor irreversibilities. Meanwhile, the increased temperature difference for heat transfer on the high-temperature side results in greater entropy generation, which further reduces the system efficiency and increases exergy losses.

Among the three candidates, R1233zd(E) exhibits superior overall performance across the entire temperature range, featuring a higher COP, lower W_c, and consistently leading exergy efficiency. At an evaporation temperature of 20 °C and a condensation temperature of 60 °C, the COP of R1233zd(E) reaches 4.85 and the cycle exergy efficiency is 9.82%, both of which are the highest among the compared working fluids. These results indicate that R1233zd(E) can satisfy the near-atmospheric operating requirement of the battery enclosure while providing both high cooling capacity and high exergy efficiency.

4.4.2 Extended comparison with typical refrigerants

Further comparisons were conducted between the three candidate working fluids and conventional refrigerants, including difluoromethane (R32), 1,1,1,2-tetrafluoroethane (R134a), and the near-azeotropic blend of difluoromethane and pentafluoroethane (R410A), to examine differences in COP, compressor power consumption (W_c), and exergy performance over the same condensation-temperature range. As shown in Fig. 12, increasing the condensation temperature leads to a decrease in COP and an increase in W_c for all refrigerants; however, the candidate fluids consistently exhibit higher COP and lower W_c overall. Figure 13 further shows that the candidate fluids achieve lower total system exergy destruction and higher exergy efficiency. These advantages are closely related to their cycle characteristics: the candidate fluids can undergo evaporative phase change near atmospheric pressure and require relatively lower condensing pressures, thereby reducing the cycle pressure lift and compressor work demand. This, in turn, improves operational stability and overall efficiency. Among the three candidates, R1233zd(E) delivers the best performance.

To identify the major sources of irreversibility, Fig. 14 compares the exergy efficiency and the component-wise shares of exergy destruction for the conventional refrigerant R134a and the proposed working fluid R1233zd(E). The

results indicate that, for both refrigerants, exergy destruction is primarily concentrated in the condenser and the compressor. For R1233zd(E), the condenser accounts for 52.6% of the total exergy destruction and the compressor accounts for 18.1%, while the expansion valve and evaporator contribute 11.5% and 7.9%, respectively; the overall system exergy efficiency is 9.8%. In contrast, the exergy efficiency of R134a is only 6.8%, and the evaporator and expansion valve contribute relatively larger fractions. This distribution suggests that heat transfer on the high-temperature side is the dominant source of exergy loss. Accordingly, improving compressor isentropic efficiency and optimizing pressure-ratio control can effectively reduce compression-related irreversibility. Moreover, incorporating internal heat recovery, expansion work recovery, or other loss-reduction measures in engineering applications may further enhance the system exergy efficiency.

Overall, the thermodynamic evaluation, from both energy utilization and exergy-loss perspectives, confirms the performance advantages of R1233zd(E) under typical battery thermal management conditions, consistent with the design objectives of near-atmospheric evaporation and low pressure-lift operation.

5. Conclusion

This study proposes a gas-immersion-enabled active safety protection concept for lithium iron phosphate battery thermal runaway by coupling an atmospheric-pressure, near-ambient phase-change refrigeration cycle with atmosphere control in a sealed battery enclosure. The concept integrates phase-change cooling, refrigerant-gas inerting, and vent-gas separation. Its feasibility was evaluated through refrigerant screening, explosion-limit tests, single-cell thermal runaway experiments, gas-liquid separation simulations, and thermodynamic analysis. The main conclusions are as follows:

(1) A closed-loop protection concept was developed using a non-flammable refrigerant as both the cooling medium and the inerting gas. The selected refrigerant evaporates near atmospheric pressure and near ambient temperature, enabling latent-heat cooling in the liquid cold plate while maintaining a non-flammable atmosphere in the enclosure. During thermal runaway, the refrigerant vapor is designed to entrain vent gases into the refrigeration loop, where combustible non-refrigerant gases can be separated and discharged.

(2) Explosion-limit tests confirmed the inerting capability of R1233zd(E) for hydrogen-containing mixtures. As the volumetric fraction of R1233zd(E) increased, the flammability range of the R1233zd(E)/H_2/air mixture narrowed markedly. When the R1233zd(E) fraction exceeded 95%, no explosion or combustion response was observed under the tested conditions, indicating effective suppression of hydrogen combustion.

(3) Single-cell thermal runaway experiments on a 28 Ah $LiFePO_4$ cell demonstrated the flame-suppression effect of

the tested refrigerant atmosphere. In open air, the vented gases were ignited and burned for approximately 302 s, with the peak temperature above the safety valve reaching 781.2 °C. In contrast, under the high-concentration R1233zd(E), oxygen-deficient sealed-chamber condition, no visible flame was observed after repeated ignition attempts, and the peak temperature above the safety valve was 88.8 °C. These results support the feasibility of suppressing secondary flaming combustion of vented gases from a single $LiFePO_4$ cell. Gas-composition analysis indicates that the vent gases consist of combustible species (e.g., H_2 and CO) and nonflammable components (e.g., CO_2), with H_2 being dominant. This further highlights the importance of reducing oxygen concentration via inerting to suppress hydrogen-containing vent-gas combustion and reduce the risk of secondary flaming combustion or deflagration in a confined enclosure.

(4) Numerical simulations under 60 °C and 0.4 MPa show that the two-phase flow field in the separator remains relatively uniform. Under gravity, the gas and liquid phases form a stable stratified structure with a clear and continuous interface. These results confirm that the separator can continuously separate liquid refrigerant from thermal runaway vent gases, thereby supporting closed-loop refrigerant circulation and sustaining a high refrigerant concentration in the sealed enclosure.

(5) Thermodynamic analysis showed that R1233zd(E) exhibited the best overall cycle performance among the candidate working fluids. At an evaporation temperature of 20 °C and a condensation temperature of 60 °C, R1233zd(E) achieved a coefficient of performance of 4.85 and a cycle exergy efficiency of 9.82%. These results indicate that R1233zd(E) is well matched to the near-atmospheric, near-ambient phase-change operating window required by the proposed protection concept.

Conflicts of interest

There are no conflicts of interest to declare.

Data availability

The data that support the findings of this study are available from the corresponding author upon reasonable request.

Acknowledgements

This study has been supported by the National Key R&D Program of China (No. 2023YFB4102202), and the Hebei Province Higher Education Institutions Scientific Research Project (No. BJ2025002).

References

1. M. H. Taabodi, T. Niknam, S. M. Sharifhosseini, H. Asadi Aghajari and S. Shojaeiyan, *J. Power Sources*,

View Article Online
DOI: 10.1039/D6EB00047A

2025, **641**, 236832.

2. K. R. Ngoy, V. T. Lukong, K. O. Yoro, J. B. Makambo, N. C. Chukwuati, C. Ibegbulam, O. Eterigho-Ikelegbe, K. Ukoba and T.-C. Jen, *Renewable and Sustainable Energy Reviews*, 2025, **223**, 115971.

3. H. Wang, Q. Wang, Z. Zhao, C. Jin, C. Xu, W. Huang, Z. Yuan, S. Wang, Y. Li, Y. Zhao, J. Sun and X. Feng, *Journal of Energy Chemistry*, 2023, **84**, 162–172.

4 J. Zhang, F. Li, L. Yu, Y. Wang, K. Wang, C. Chang, M. Li, W. Hao and X. Qian, *Chemical Engineering Journal*, 2025, **505**, 159699.

5 J. Zhao, L. Ma, L. Zhao, J. Zhang and T. Xu, *J. Energy Storage*, 2025, **133**, 117925.

6 M. Calabrese, M. Portarapillo, A. Di Nardo, V. Venezia, M. Turco, G. Luciani and A. Di Benedetto, *Energies (Basel).*, 2024, **17**, 1350.

7 G. Li, M. Niu, J. Jian and Y. Lu, *Renewable and Sustainable Energy Reviews*, 2025, **213**, 115411.

8 D. Kong, H. Lv, P. Ping and G. Wang, *J. Energy Storage*, 2023, **64**, 107073.

9 W. Mei, Z. Liu, C. Wang, C. Wu, Y. Liu, P. Liu, X. Xia, X. Xue, X. Han, J. Sun, G. Xiao, H. Tam, J. Albert, Q. Wang and T. Guo, *Nat. Commun.*, 2023, **14**, 5251.

10 X. Feng, D. Ren, X. He and M. Ouyang, *Joule*, 2020, **4**, 743–770.

11 F. S. Hwang, T. Confrey, C. Reidy, D. Picovici, D. Callaghan, D. Culliton and C. Nolan, *Renewable and Sustainable Energy Reviews*, 2024, **192**, 114171.

12 R. Zhou, Y. Chen, J. Zhang and P. Guo, *Mater. Adv.*, 2023, **4**, 4011–4040.

13 Z. Tian, Z. Huang, Y. Zhou, Z. Cao and W. Gao, *Appl. Therm. Eng.*, 2024, **236**, 121571.

14 A. Wahab, A.-U.-H. Najmi, H. Senobar, N. Amjady, H. Kemper and H. Khayyam, *Renewable and Sustainable Energy Reviews*, 2025, **211**, 115268.

15 S. K. Wong, K. Li, X. Rui, L. Fan, M. Ouyang and X. Feng, *Energy*, 2024, **307**, 132353.

16 X. Sun, Y. Dong, P. Sun and B. Zheng, *J. Energy Storage*, 2024, **76**, 109812.

17 M. Chen, M. Zhu, L. Zhao and Y. Chen, *Appl. Energy*, 2024, **367**, 123394.

18 X. Shen, Q. Duan, P. Qin, Q. Wang and J. Sun, *Energy Storage Science and Technology*, 2023, **12**, 1862–1871.

19 V. Talele, M. S. Patil, S. Panchal, R. Fraser and M. Fowler, *J. Energy Storage*, 2023, **65**, 107253.

20 J. Hu, X. Tang, X. Zhu, T. Liu and X. Wang, *Energy*, 2024, **286**, 129669.

21 I. Dhuchakallaya and P. Saechan, *J. Energy Storage*, 2024, **101**, 113916.

22 D. Jie, C. Baohui, L. Jiazheng, Z. Tiannian and W. Chuanping, *J. Energy Storage*, 2024, **103**, 114290.

23 Y. Hong, B. Zang, D. Yao, X. Gao, J. Chen, C. Lu and X. Pang, *Chemical Engineering Journal*, 2025, **521**, 166639.

24 H. Sun, G. Li and C. Yuan, *Chemical Engineering Journal*, 2025, **525**, 170166.

25 K. O. A. Amano, S.-K. Hahn, N. Butt, P. Vorwerk, E. Gimadieva, R. Tschirschwitz, T. Rappsilber and U. Krause, *Batteries*, 2023, **9**, 300.

26 E. Brandes, V. Schroeder and J. Milde, *PTB-Mitteilungen*, 2011, **121**, 1.

27 H. Miao, L. Lu and Z. Huang, *Int. J. Hydrogen Energy*, 2011, **36**, 6937–6947.

28 Y. Zhao, F. Zhao, C. Li, W. Wang, R. Li, J. Li, P. Yang and Y. Liu, *International Communications in Heat and Mass Transfer*, 2025, **167**, 109409.

29 H. Zhang, T. Bai and Z. Wen, *Appl. Therm. Eng.*, 2025, **281**, 128518.

30 G. Wei, R. Huang, G. Zhang, B. Jiang, J. Zhu, Y. Guo, G. Han, X. Wei and H. Dai, *Appl. Energy*, 2023, **349**, 121651.

31 Y. Zhang, T. Mo, X. Wu, H. Yu and B. Mao, *J. Power Sources*, 2026, **662**, 238780.

32 C. Qi, Z. Liu, C. Lin, X. Liu, D. Liu, Z. Li and A. Yi, *J. Energy Storage*, 2024, **88**, 111678.

33 A. Du Pasquier, F. Disma, T. Bowmer, A. S. Gozdz, G. Amatucci and J. -M. Tarascon, *J. Electrochem. Soc.*, 1998, **145**, 472–477.

34 K. Zou, K. He and S. Lu, *Int. J. Heat Mass Transf.*, 2022, **195**, 123133.

35 Q. Zhang, W. Song, G. Zhou, J. Wang, H. Lu, B. Guo, J. Zhao, T. Liang, M. Zhang, Y. Kong and Q. Liu, *Appl. Therm. Eng.*, 2025, **279**, 127988.

36 R. Spotnitz and J. Franklin, *Journal of Power Sources*, 2003, **113**, 81–100.

View Article Online
DOI: 10.1039/D6EB00047A

Table 1 Physical data for selected refrigerants

Refrigerant	NBP(°C)	Critical temp(°C)	Critical press(MPa)	ODP	GWP(100)	Safety level
R1233zd(E)	18.263	166.45	3.6237	0.00034	1	A1
R1224yd(Z)	14.617	155.54	3.337	0.00023	0.88	A1
R245fa	15.048	153.86	3.651	0	1030	B1

View Article Online
DOI: 10.1039/D6EB00047A

Table 2 Verification of explosion limit experimental data

	This study	Reference[27]	Relative Difference
Conditions	30°C/dry air 6 L chamber	ambient temperature 5.34 L chamber	
LEL	5.011%	5%	0.22%
UEL	74.577%	76.5%	2.51%

View Article Online
DOI: 10.1039/D6EB00047A

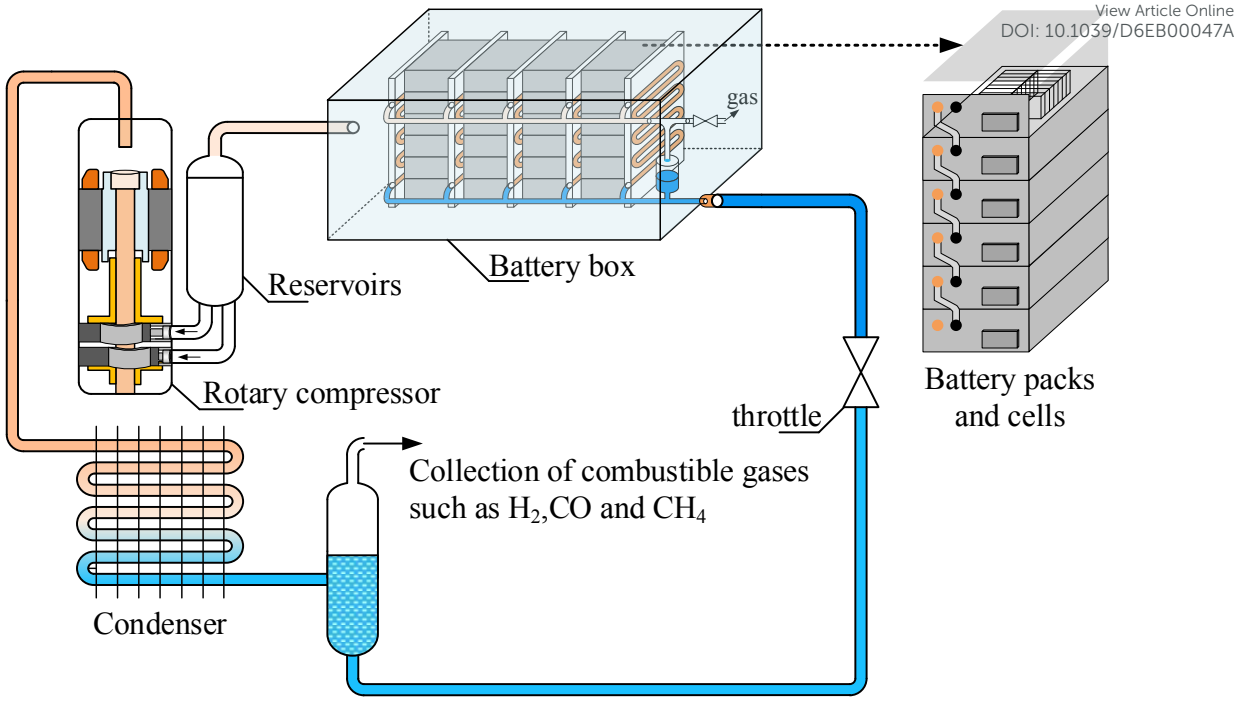

Fig. 1. Schematic of the proposed active protection system.

View Article Online
DOI: 10.1039/D6EB00047A

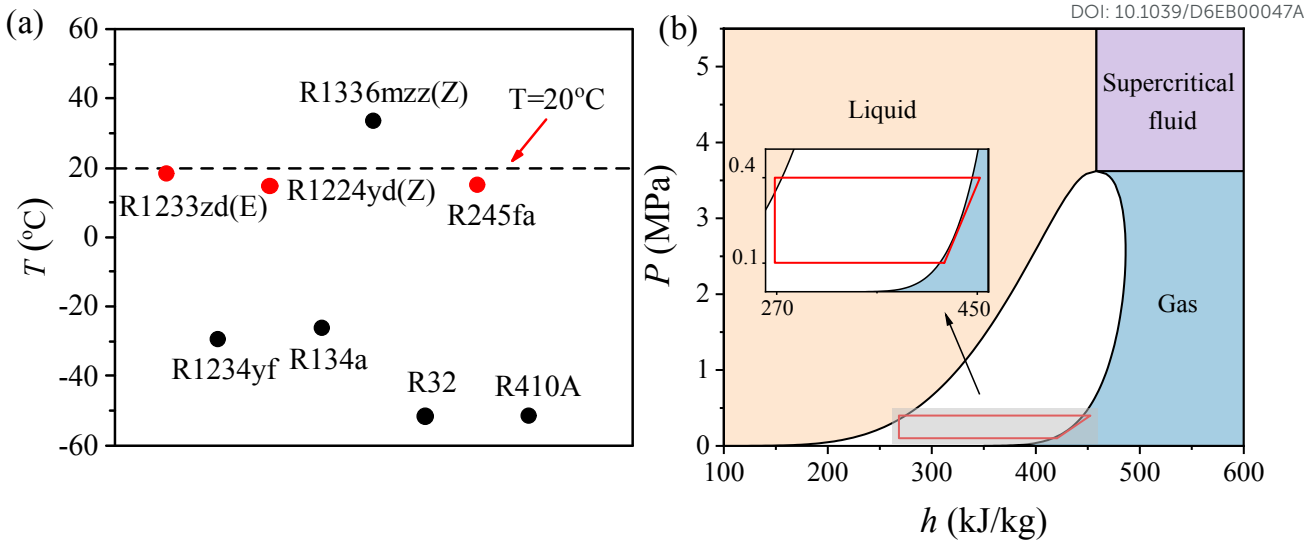

Fig. 2. (a) Screening of candidate refrigerants; (b) three-phase diagram of R1233zd(E) and P-h diagram of the vapor-compression refrigeration cycle.

View Article Online
DOI: 10.1039/D6EB00047A

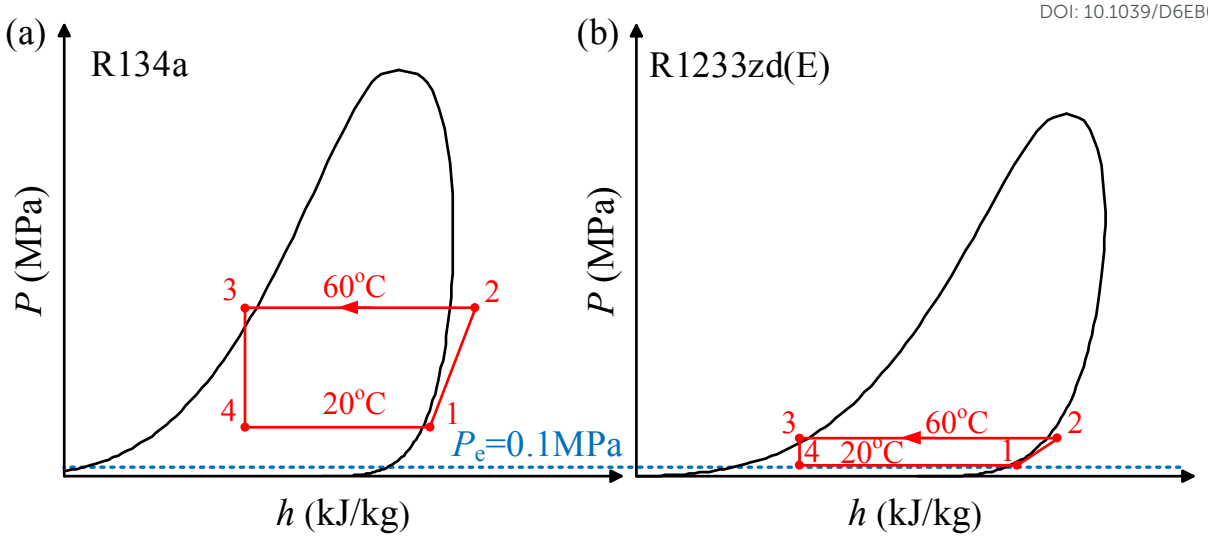

Fig. 3. (a) Conventional closed cycle; (b) Near-atmospheric-pressure coupled cycle.

View Article Online
DOI: 10.1039/D6EB00047A

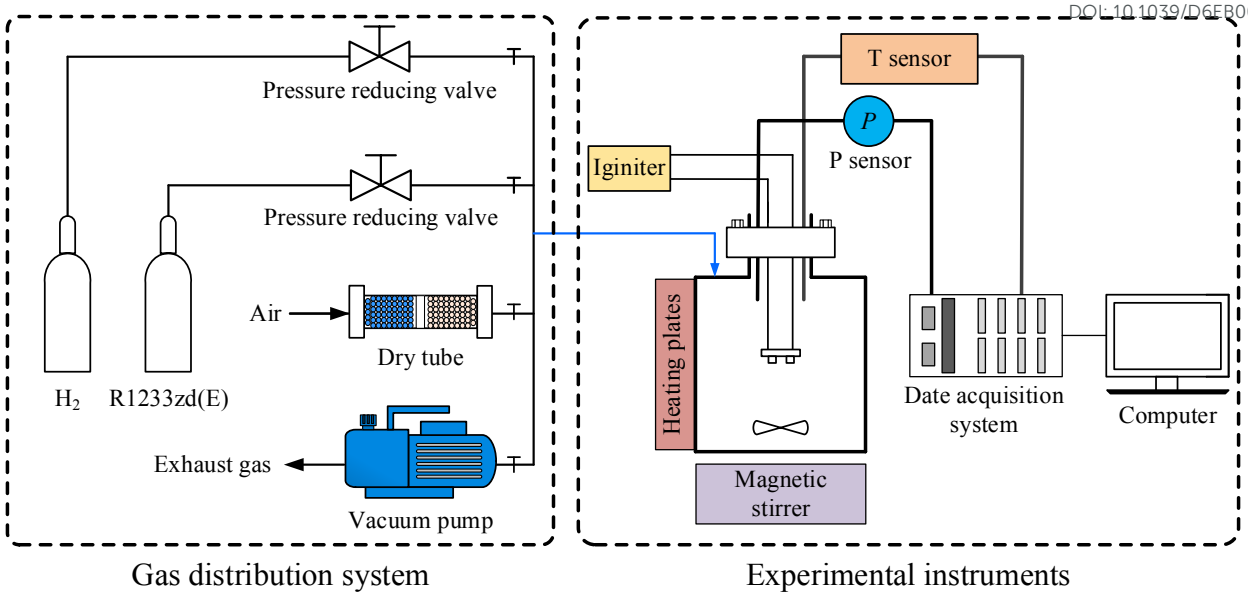

Fig. 4. Explosion-limit test apparatus.

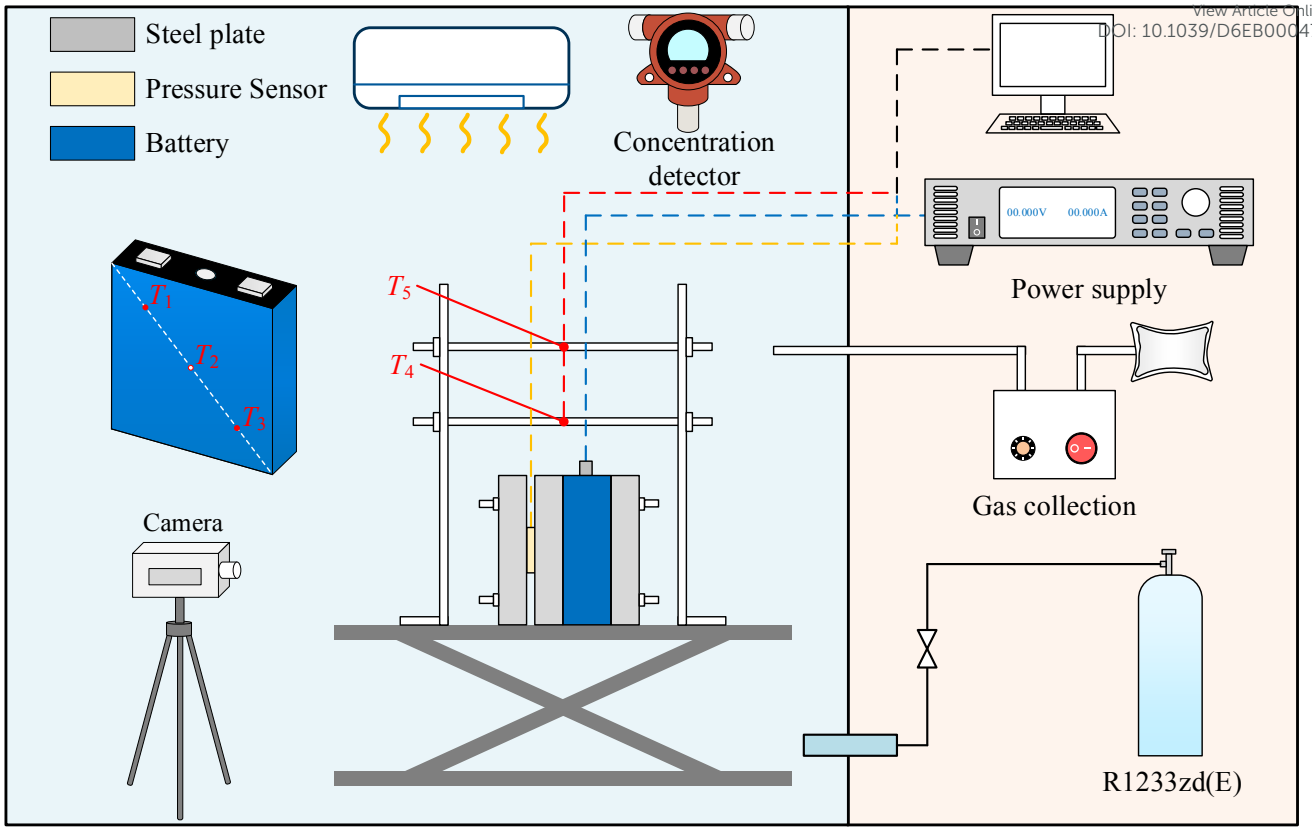

Fig. 5. Experimental setup for battery thermal runaway.

View Article Online
DOI: 10.1039/D6EB00047A

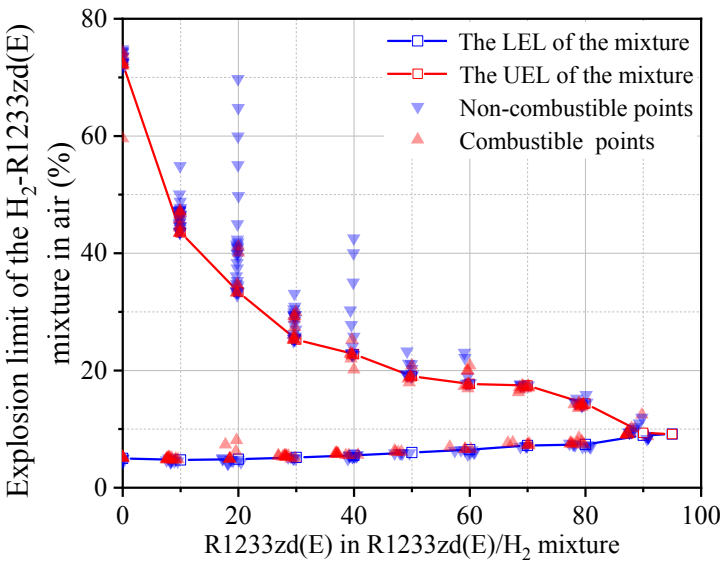

Fig. 6. Explosion limits of the mixture at different R1233zd(E)-H_2 volume fractions.

View Article Online
DOI: 10.1039/D6EB00047A

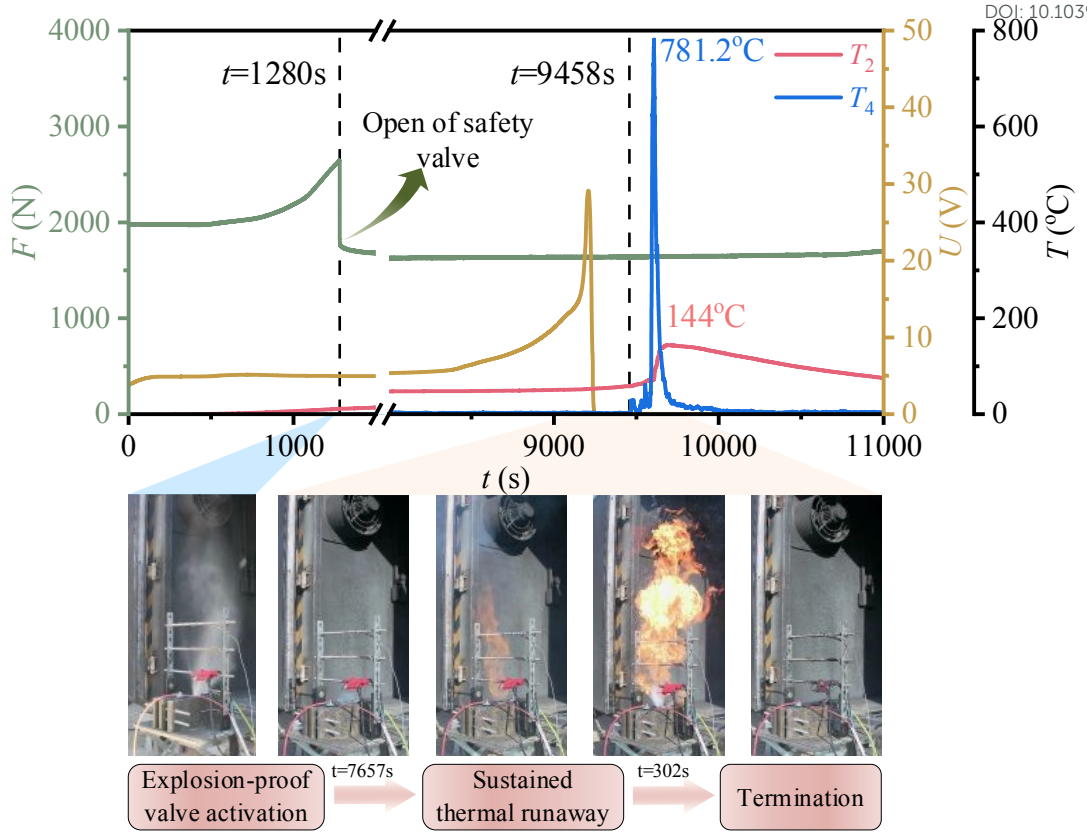

Fig. 7. Temperature, expansion force, and voltage responses during thermal runaway under an air atmosphere.

View Article Online
DOI: 10.1039/D6EB00047A

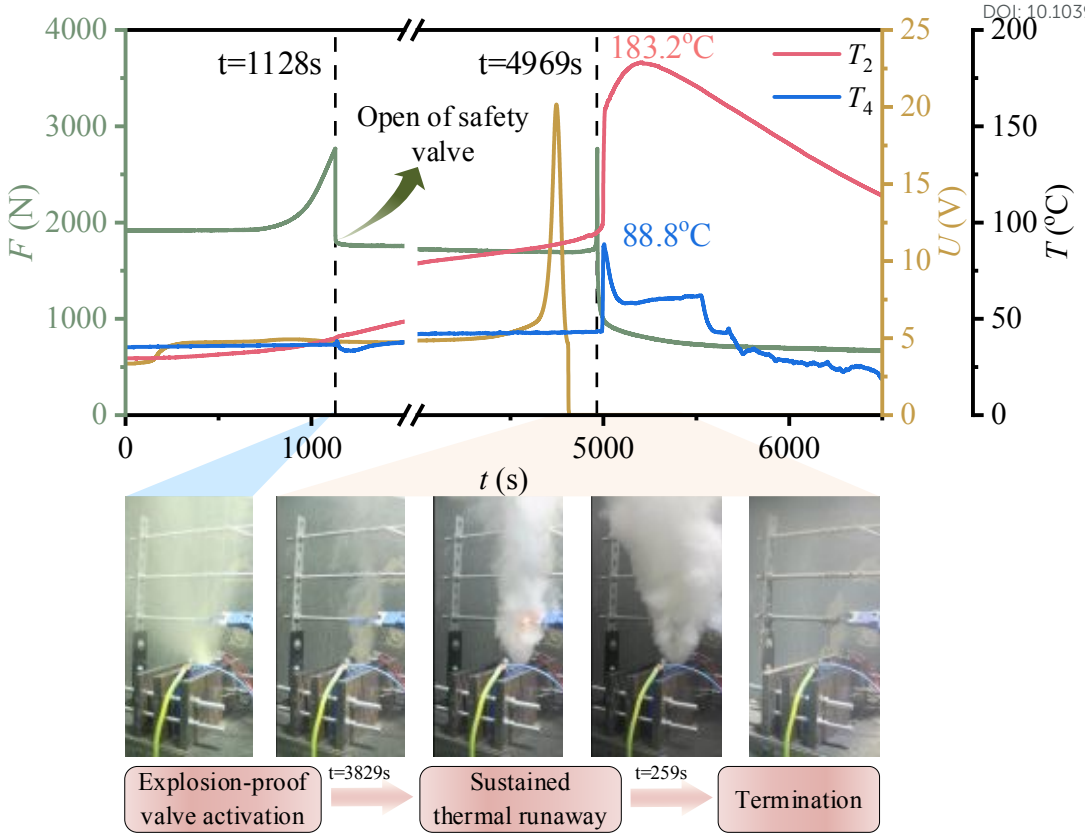

Fig. 8. Temperature, expansion force, and voltage responses during thermal runaway under an R1233zd(E) atmosphere.

View Article Online
DOI: 10.1039/D6EB00047A

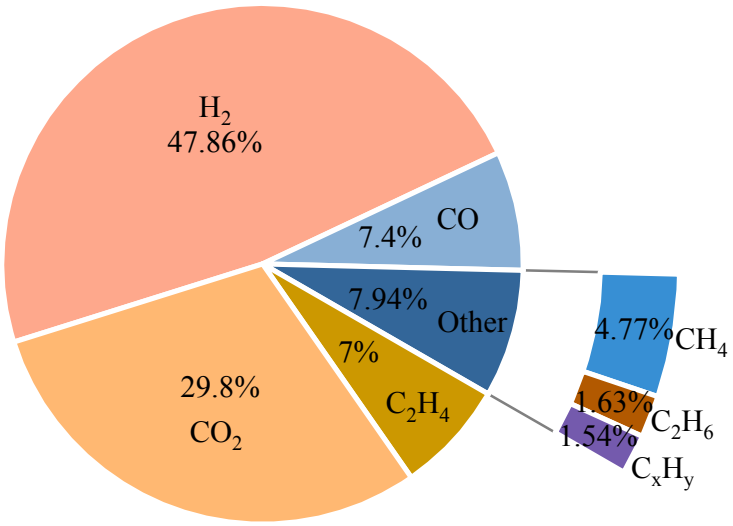

Fig. 9. Composition of gases generated during thermal runaway.

View Article Online
DOI: 10.1039/D6EB00047A

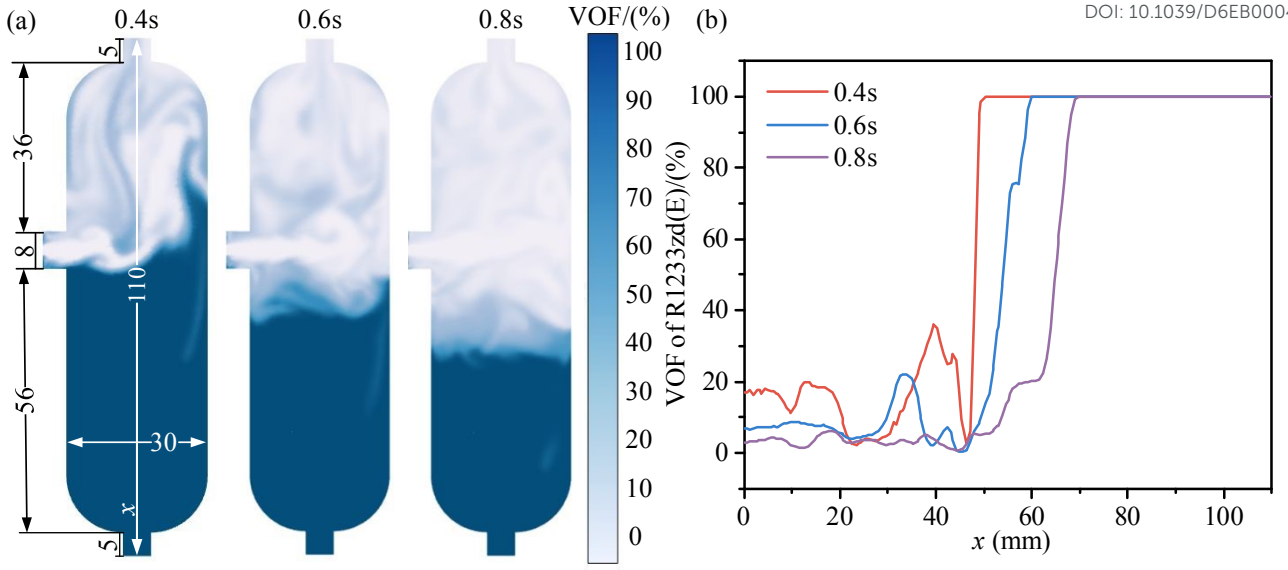

Fig. 10. (a) Contours of the volumetric fraction of R1233zd(E); (b) axial distribution of the R1233zd(E) volumetric fraction along the centerline at different times.

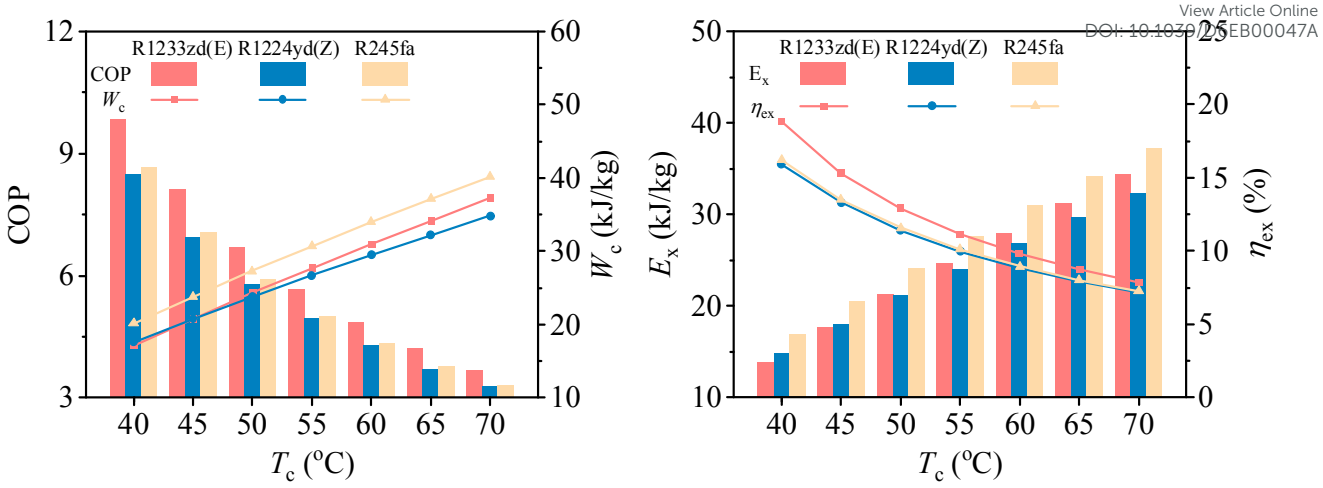

Fig. 11. First- and second-law performance comparison of the three candidate working fluids.

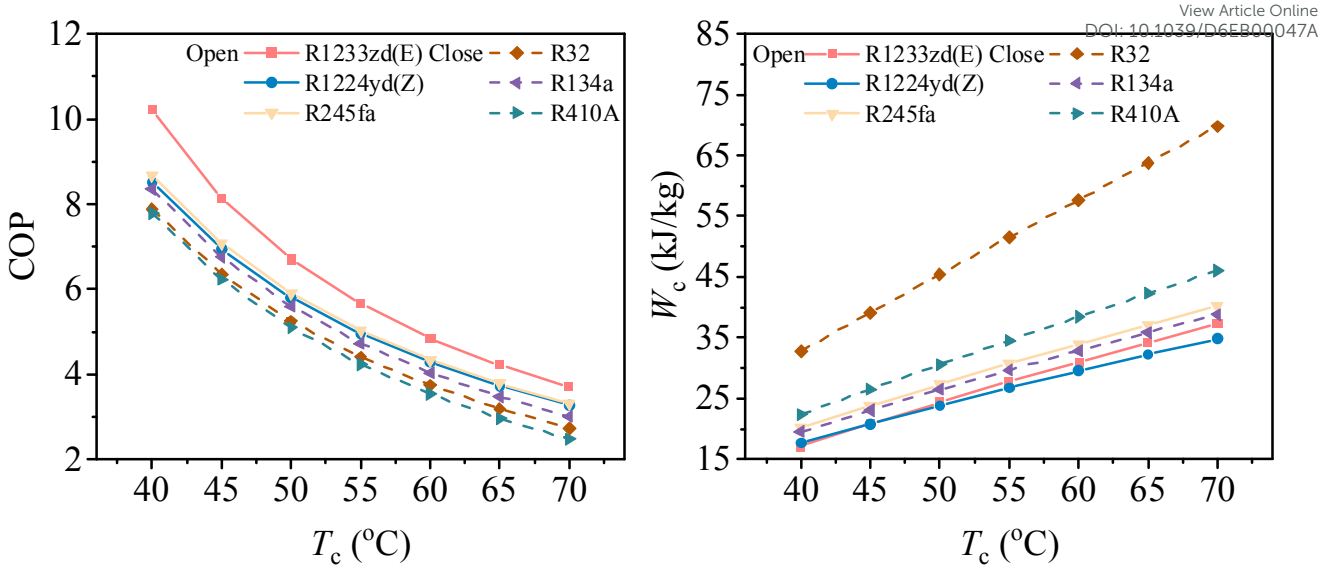

Fig. 12. Comparison of COP and W_c for seven working fluids.

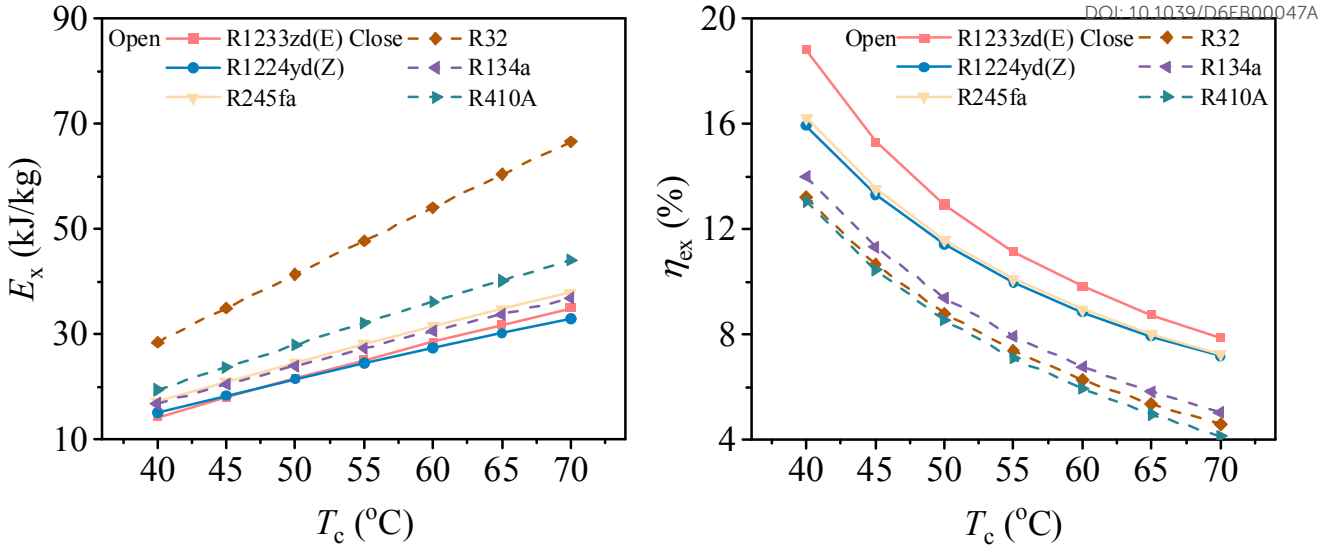

Fig. 13. Comparison of total system exergy destruction and exergy efficiency for seven working fluids.

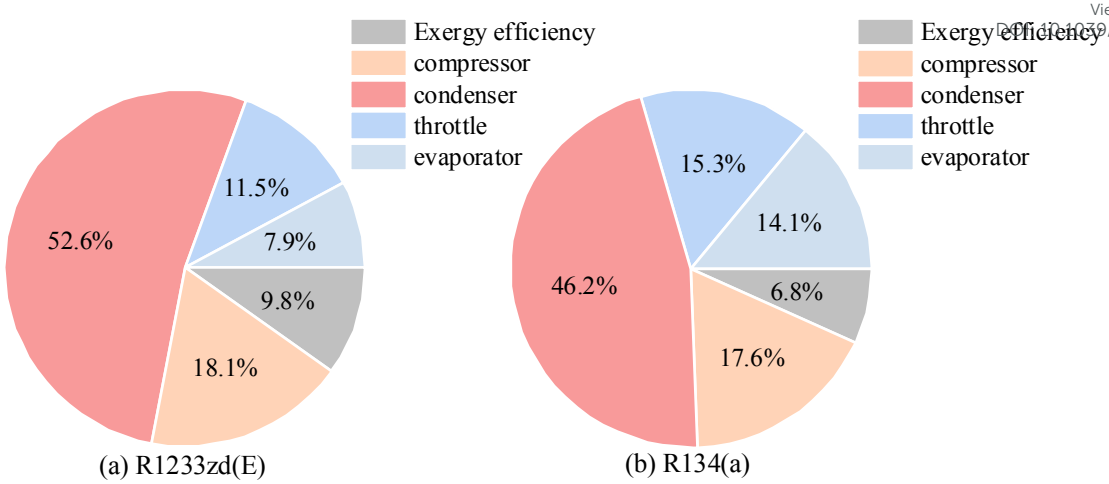

Fig. 14 Component-wise exergy destruction shares and overall exergy efficiency for the R134a and R1233zd(E) cycles.

View Article Online
DOI: 10.1039/D6EB00047A

Data availability

The data supporting the findings of this study are available within the article and its supplementary materials. Further raw data are available from the corresponding author upon reasonable request.